Journal of Marine Science and Application (2025) 24: 1075-1085
https://doi.org/10.1007/s11804-025-00614-7

RESEARCH ARTICLE

Wave-Driven Energy Harvesting from Frequency-Increasing Floating Structures

Mir Mohammad Ettefagh[1], Alireza Hesari[1], Reza Fathi[1] and Sina Akhbari[2]

Received: 06 January 2024 / Accepted: 26 January 2025

Abstract

This study focuses on wave energy harvesting by leveraging the impact-induced frequency of sea waves. It introduces a novel double-buoyed model based on the existing single-buoyed system to address the shortcomings of previous systems. Notably, the traditional single-buoyed system, which is characterized by a long beam extending to the sea floor, proves impractical in deep-sea environments, especially in distant offshore regions. The proposed double-buoyed model replaces the long beam with a second buoy to increase energy harvesting efficiency. A parametric analysis that included the density and height of the first buoy and wave period was conducted to enhance the proposed model further. Results indicated that with the selection of optimal parameters, the power output of the double-buoyed system increased by approximately 13-fold, thereby enhancing the viability and efficiency of wave energy harvesting.

Keywords Energy harvesting; Sea wave; Buoy; Piezoelectricity; Impact

1 Introduction

As scientific exploration and human curiosity continue to expand, the frontiers of research have extended beyond terrains to involve the vast sea. This expansion necessitates an in-depth examination of marine life and the characteristics of sea waves within the water and at its surface. Various sensors play an important role in advancing marine engineering (Falnes and Kurniawan, 2020). However, beyond the challenges associated with manufacturing these instruments, their power source has raised substantial concern. The application of energy harvesting systems is a new approach for powering the low-power electronic devices implemented in the sea. In this method, piezoelectric materials are used for converting the mechanical energy of sea waves into electrical energy. This method has the advantage of not using battery charging systems (Jahangiri et al., 2016). Batteries are the primary energy sources for wireless sensors. However, they present several limitations. For example, their weight can detrimentally affect sensor performance. Moreover, their finite lifespan increases maintenance costs, and their weakness in diverse temperature and weather conditions poses operational challenges. Consequently, scientists have directed growing attention to optimizing batteries in terms of their weight and performance, with a united effort to explore means of recharging batteries without necessitating their replacement. The conversion of diverse energy forms into electrical energy for applications in compact dimensions is a key focus in cutting-edge research (Xu et al., 2014).

Researchers employ various methods, including the application of magnetic force and impact and etc. (Mohapatra and Guedes Soares, 2024), to harness energy from sea waves and convert it into electrical power. Hoffmann et al. (2016) introduced the concept of self-adjusting energy, which is characterized by the ability of devices to adapt to specific frequencies under operational conditions. In this approach, sea waves separate two magnets, generating a magnetic flux that produces electricity. Xie and Wang (2017a) proposed an ocean wave energy harvester made of a composite piezoelectric buoy structure. They provided a more practical and efficient method for harvesting ocean wave energy by implementing of composite piezoelectric

Article Highlights

- A novel double-buoyed mechanical device is proposed for wave energy harvesting.
- This device is based on impacts between beams with piezoelectric layers and moving teeth.
- A mathematical model of the system is constructed considering the fluid structure interaction between the buoy and the wave.
- The selection of optimal parameters for the system leads to increasing generated power significantly.

✉ Mir Mohammad Ettefagh
ettefagh@tabrizu.ac.ir

[1] Department of Mechanical Engineering, University of Tabriz, Tabriz 5166616471, Iran

[2] Intelligent Automation Centre, Wolfson School of Mechanical, Electrical & Manufacturing Engineering, Loughborough University, Loughborough LE11 3TU, UK

structures. In a separate study, researchers proposed a mechanism analogous to a gearbox, employing two gears to amplify motion power, thus expanding the range of wave movement by up to six times. This mechanism, which comprises two rotors and one shoulder gear, leverages the difference in gear diameters to enhance its power output, ultimately amplifying piezoelectric power (Chen et al., 2021). Xie et al. (2014) investigated the energy harvesting from transverse ocean waves by a piezoelectric plate. They developed harvester which is made of two horizontal cantilever plates with piezoelectric patches and fixed on a vertical rectangular column. Moreover, Wu et al. (2015) presented an expedient piezoelectric coupled buoy energy harvester. This harvester, which features a slender cylindrical floater on a large sinker, facilitates the conversion of transverse ocean wave energy into electrical energy through piezoelectric patches mounted on cantilevers. Nan et al. (2021) presented a magnet-free bistable piezoelectric energy harvester designed for sustainable power generation from ambient vibrations to support microelectronics. Their design features a predeformed sinusoidal beam with integrated piezoelectric layers and a U-shaped torsion device. An approach proposed by Xie and Wang (2017b) involves the application of a composite cylinder. This method uses a rotor–stator system, where the stator is shaped as an octagon with single-jointed beams attached to its sides. Concentrated masses in the form of magnets are positioned at the free ends of the beams. A robust magnet is mounted on the rotor bar, and the rotor induces vibration in the beams as it undergoes rotation with the positive and negative poles positioned around the rotor rod. Ramezanpour et al. (2016) introduced an alternative model employing a rotating pendulum connected to a concentrated mass on a plane, with the sea wave acting as the driving force for the pendulum. Another method (Lin and Zhang, 2016) involves a rigid, fixed beam anchored to the seabed, with several single-ended beams using small piezoelectric patches embedded in their bodies. Additionally, a hollow cylindrical buoy with rigid teeth on its inner wall has been employed. The motion of sea waves propels the buoy along the rigid beam, causing the teeth to impact the supporting beams and generate high-frequency vibrational motion. This approach transforms the low-frequency vibrations of sea waves (0.03–10 Hz) into high-frequency ones, facilitating the conversion of mechanical energy into electrical energy. However, Mirab et al. (2015) introduced an approach to power low-energy electronic devices at sea by employing piezoelectric materials. Moreover, they implemented the JONSWAP wave model and optimized parameters with a simulated annealing algorithm. Chen et al. (2022) explored the use of chaotic vibrations for enhancing energy harvesting, focusing on a piezoelectric wind energy harvester with a magnetic chaotic pendulum. They utilized particle swarm optimization in conjunction with a neural network to optimize the output power of the proposed structure. In a separate research, Bao et al. (2022) investigated multiphase flow-induced vibration energy harvesting. The proposed piezoelectric harvester, by utilizing air–water two-phase flow and a T-shaped cantilever, captures liquid sloshing energy. Du et al. (2024a) developed a wake galloping piezoelectric–electromagnetic hybrid energy harvesting mechanism to harvest electric power from ocean wave energy. This mechanism is composed of an air chamber intake for the oscillating water column and a piezoelectric–electromagnetic hybrid waves energy harvester in a vortex tunnel. Du et al. (2024b) proposed a multipillar piezoelectric stack device for harvesting ocean wave energy. This device utilizes a unique rack, pinion, and cam system to convert the heaving motion of floats into a unidirectional rotation. Wang et al. (2024) provided a comprehensive review of technologies that have been employed in recent years to harvest energy from marine fluids by using water kinetic piezoelectric energy harvesters.

Each of the aforementioned concepts possesses a set of advantages and disadvantages, and the advantages of a specific approach cannot be universally regarded as superior or inferior to those of other methods. The majority of researchers have focused on enhancing the efficacy of these concepts. For instance, as reported by Lin and Zhang (2016), the depth of the sea varies across its bed, posing challenges to certain systems where the required sea depth is impractically high or the expense of connecting a long beam to the seabed becomes unreasonable. Consequently, the primary objective of the present study is to introduce a new energy harvesting system. This novel approach involves the substitution of a second buoy for a rod connected to the seabed, thereby reducing the limitations associated with previous systems.

The rest of this paper is organized as follows: Section 2 details the dynamic modeling of the proposed system, outlining formulations, the numerical simulation algorithm, and motion segmentation. Section 3 centers on discussing the results of simulations and parametric analyses, which encompass variations in the density of the first buoy, as well as buoy diameter, wave period, and height. The effect of each parameter on the proposed system's behavior and harvested energy is discussed in detail. Finally, the paper is concluded in Section 4.

2 Dynamic simulation of the double-buoyed structure

Figure 1(a) illustrates that the viability of single-buoyed systems is primarily constrained to ideal conditions, such as a laboratory wave pool simulating a shallow water environment. Consequently, the primary objective of the present study is to propose a system similar to the model depicted

in Figure 1(b). This novel approach involves the substitution of a second buoy for a rod connected to the seabed, thereby reducing the limitations associated with previous systems. In this configuration, the second buoy, alongside the initial buoy, possesses the capability to move in conjunction with sea waves, thus enhancing the adaptability and robustness of the proposed system.

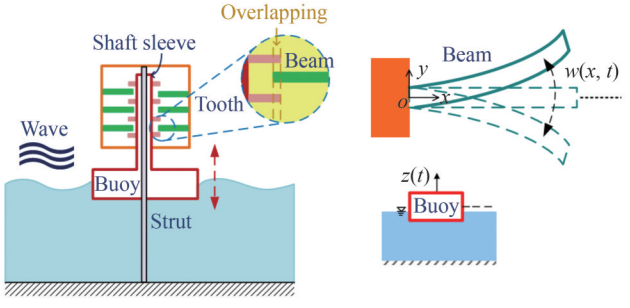

(a) Single-buoyed system (Lin and Zhang, 2016)

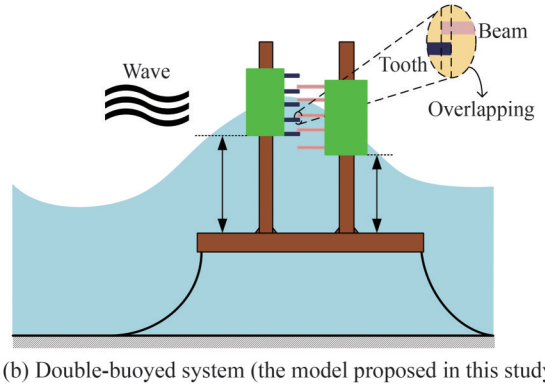

(b) Double-buoyed system (the model proposed in this study)

Figure 1 Schematic representation of the system for harvesting energy from sea waves

The purpose of dynamic simulation is to optimize system output and thus enhance energy harvesting. The simulation of system behavior provides a comprehensive understanding of the effect of each parameter. After the analysis of each parameter, adjustments can be made to enhance overall system efficiency.

Figure 1(b) illustrates that the arrangement of teeth and cantilever beams has been transferred onto the external surfaces of two buoy cylinders. The mobility of the two buoys is constrained to motion along separate parallel guide rods situated on a single plane. The assembly is tied to the seabed via cables. The dynamic interaction between the rigid teeth and vibrating beams is augmented by the increased relative speed facilitated by the movement of the two buoys, resulting in an impact velocity that is higher than that produced by a beam in a fixed state. The spatial separation between the buoy lines ensures a consistent phase difference in the movement of the two buoys as a wave traverses the system. The accurate design and optimization of the proposed system for enhanced energy harvesting require comprehensive system modeling and simulation. Therefore, a primary objective of this study is the dynamic simulation of the double-buoyed system designed to increase the frequency of impact for improved energy harvesting from sea waves, thus addressing the limitations of previous systems. Mathematical modeling involves deriving the equations of motion for the two buoys and the beam. It is followed by the numerical solution of these equations through coding in the MATLAB software environment.

2.1 Dynamic modeling

The motion of two buoys occurs in parallel cause colliding due to the interaction between a tooth and beam. Consequently, the governing equations of system consist of two distinct states: The first corresponds to instances when no collision occurs, resulting in the free vibrations of the beam. The second involves forced vibrations, expressed as a coupled motion between the cantilever beam and buoys during collisions between the beam and tooth. The following dynamic equations apply to the state of free vibrations (Lin and Zhang, 2016):

$$\left(m_{f1}+m_{f1\infty}\right)\ddot{Z}_{f1}(t)+c_{f1b}\dot{Z}_{f1}(t)+k_{f1}Z_{f1}(t)+\int_0^t K_{f1}(t-\tau)\dot{Z}_{f1}(\tau)\mathrm{d}\tau=F_{f1w}\sin(2\pi t/T) \tag{1a}$$

$$\left(m_{f2}+m_{f2\infty}\right)\ddot{Z}_{f2}(t)+c_{f2b}\dot{Z}_{f1}(t)+k_{f2}Z_{f2}(t)+\int_0^t K_{f2}(t-\tau)\dot{Z}_{f1}(\tau)\mathrm{d}\tau=F_{f2w}\sin\left(2\pi t/T+\varphi\right) \tag{1b}$$

$$\mu\ddot{w}(x,t)+c_v\dot{w}(x,t)+EIw''''(x,t)=0 \tag{1c}$$

Equation (1a) refers to the first buoy (tooth carrier). Equation (1b) is related to the second buoy (beam carrier). Equation (1c) represents a cantilever beam of the Euler–Bernoulli type. In the event of a collision between the tooth and beam, the impact is incorporated into the second side of the equation, resulting in the following conjugate equations (Lin and Zhang, 2016):

$$\left(m_{f1}+m_{f1\infty}\right)\ddot{Z}_{f1}(t)+c_{f1b}\dot{Z}_{f1}(t)+k_{f1}Z_{f1}(t)+\int_0^t K_{f1}(t-\tau)\dot{Z}_{f1}(\tau)\mathrm{d}\tau=F_{f1w}\sin(2\pi t/T)-F_c \tag{2a}$$

$$\left(m_{f2}+m_{f2\infty}\right)\ddot{z}_{f2}(t)+c_{f2b}\dot{Z}_{f2}(t)+k_{f2}Z_{f2}(t)+\int_0^t K_{f2}(t-\tau)\dot{Z}_{f2}(\tau)\mathrm{d}\tau=F_{f2w}\sin\left(2\pi t/T+\varphi\right)-F_c \tag{2b}$$

$$\mu\ddot{w}(x,t)+c_v\dot{w}(x,t)+EIw''''(x,t)=F_c\delta(x-1) \tag{2c}$$

In Equations (1) and (2), the subscript $f1$ denotes the first buoy, and $f2$ represents the second buoy. Additionally, the

terms are defined as follows: $m_{f1\infty}$ is the added mass for the first buoy, m_{f1} is the mass of the buoy, c_{f1b} is the equivalent viscous damping coefficient of the buoy, k_{f1} is the equivalent buoyancy coefficient, $Z_{f1}(t)$ denotes the vertical displacement of the buoy, and $Z_{f1}(t-\tau)$ signifies the response of the buoy's impact function (Cummins, 1962). Furthermore, $F_{f1w}\sin(2\pi t/T)$ denotes the excitation force resulting from a wave interacting with the buoy. μ represents the mass per unit length of the beam, c_v is the damping coefficient of the beam, I stands for the second moment of the beam area, and E is the Young's modulus of the beam. F_c indicates the force resulting from the impact or adherence between the tooth and beam. φ represents the phase difference between the two buoys. δ is the Dirac delta function denoting impact, and $w(x,t)$ signifies the deflection of a single beam at a distance x from the end of the beam and time t. In these equations, the coordinate system of the reference device originates from the free surface of the water in a wave-less state, with the coordinates of the first buoy starting from the end of the tooth and those of the second buoy starting from the end of the beam.

The algorithm employed in this study for the numerical solution of the dynamic Equations (1) and (2) and simulations of the proposed system is drawn as a flowchart in Figure 2. In this algorithm, the system inputs are defined as follows: D_{f1} is the diameter of the first buoy, and D_{f2} is the diameter of the second buoy. H_{f1} is the height of the first buoy, and H_{f2} is the height of the second buoy. H_{wf1} is the wetting height of the first buoy, and H_{wf2} is the height of the wetting surface of the second buoy. R_{of1} is the density of the first buoy, and R_{of2} is the density of the second buoy. L is the length of the beam, W is the width of the beam, T is the thickness of the beam, and E is the elasticity modulus of the beam. L_{ovlp} is the amount of beam–tooth overlap. WP is the wave period, time is the total duration of the system simulation, and k is the time step counter. In terms of algorithm outputs, $Z_{2\text{abs}f1}$ represents the absolute displacement of the first buoy relative to the reference coordinate system, and $Z_{2\text{abs}f2}$ denotes the absolute displacement of the second buoy relative to the reference coordinate system. W_{rel} is the relative deflection of the beam (relative to the buoy connected to it, i.e., the second buoy), $W_{\text{relvelocity}}$ represents the relative velocity of the beam (relative to the connected buoy, i.e., the second float), and W_{abs} reflects the absolute deflection of the beam relative to the reference coordinate system. Z_{1f1} indicates the speed of the first buoy (the buoy to which the tooth is attached), and Z_{1f2} represents the speed of the second buoy (the buoy carrying the beam).

The motion of the two buoys occurs in parallel, with periodic collision due to the interaction between the tooth and beam. In other words, when the buoys are excited to heave by a wave, the tooth in the second buoy moves and collides with the free end of the beam in the first buoy. The tooth forces the beam to bend, and horizontal displacement develops at the beam tip. This state does not change until another contact occurs. The tooth and cantilever beams move independently of each other in the absence of interaction. The algorithm depicted in Figure 2 is developed to acquire the results in accordance with the abovementioned situation. The system is characterized by two distinct states: free and coupling. The coupling state between the tooth and beam is further subdivided into two states: stick-

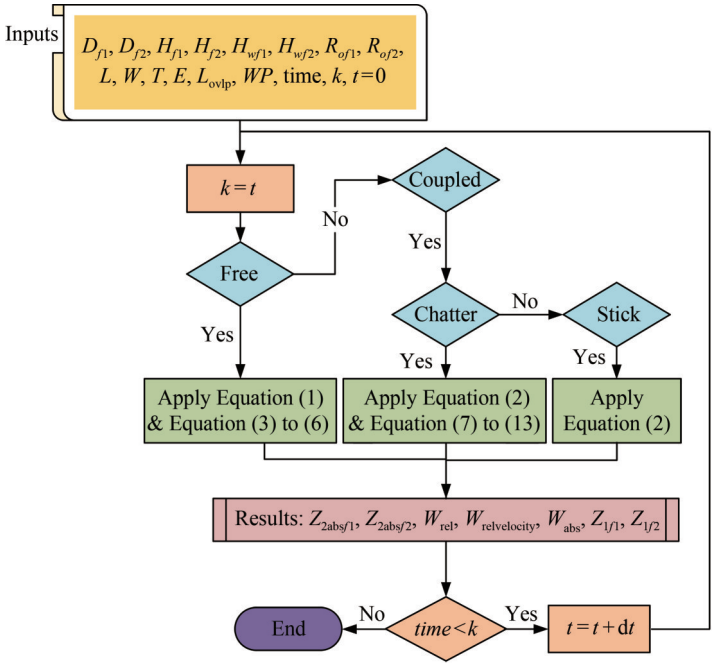

Figure 2 Flowchart of the proposed algorithm for dynamic simulation

ing and chatter. When the system is in a free state, Equation (1) is utilized. Otherwise, Equation (2) is employed. The detection of the free, chatter, and sticking states is explained in detail in the following sections.

2.2 Free state

The free state appears when the tooth and beam undergo independent motion without colliding. Given that all analyses in this study are conducted through coding in the MATLAB environment (utilizing a PC with Intel Core I7-13700, 3.4 GHz CPU, and 32 GB of RAM), the conditions defining the free state must be explicitly specified in the code. Conditional statements are employed for this purpose within the written code. As illustrated in Figure (1b), the movement of the buoys is constrained to linear motion in the vertical direction. With these considerations, two overarching states characterize the relative movement of the beam and tooth in the free state, and the associated conditions are described below.

Condition#1. The separation distance between the tooth and fixed beam end must exceed the maximum deflection of the free beam end, as indicated by the following conditions:

$$\mathrm{abs}\left(Z_{2f1}(k-1)-Z_{2f2}(k-1)\right)>\mathrm{Max}\left(W_{\mathrm{rel}}\right) \quad (3)$$

$$\mathrm{abs}\left(Z_{2f1}(k-1)-Z_{2f2}(k-1)\right)<-\mathrm{Max}\left(W_{\mathrm{rel}}\right) \quad (4)$$

where k is the time step numerator.

Condition#2. The distance between the tooth and the fixed end of the beam should be less than the maximum deflection of the free end of the beam. The origin of the coordinates is established at the water surface in a wave-less state. The distance between the tooth and the fixed end of the beam during the interval between two consecutive time steps, k and $k-1$, must exceed the distance from the head of the beam to the coordinate origin to prevent contact between the tooth and beam. If the distance at time step $k-1$ is large and that at k is small, collision has undoubtedly occurred. This condition is expressed in the following equations:

$$\begin{cases} W_{\mathrm{rel}}\left(n_{\mathrm{elem}},k-1\right)>\mathrm{abs}\left(Z_{2f1}(k-1)-Z_{2f2}(k-1)\right) \\ W_{\mathrm{rel}}\left(n_{\mathrm{elem}},k-1\right)>\mathrm{abs}\left(Z_{2f1}(k)-Z_{2f2}(k)\right) \end{cases} \quad (5)$$

$$\begin{cases} W_{\mathrm{rel}}\left(n_{\mathrm{elem}},k-1\right)<\mathrm{abs}\left(Z_{2f1}(k-1)-Z_{2f2}(k-1)\right) \\ W_{\mathrm{rel}}\left(n_{\mathrm{elem}},k\right)<\mathrm{abs}\left(Z_{2f1}(k)-Z_{2f2}(k)\right) \end{cases} \quad (6)$$

where $W_{\mathrm{rel}}\left(n_{\mathrm{elem}},k\right)$ denotes the relative deflection of the end of the cantilever beam connected to the float, specifically for the first mode of vibration at step k. Here, the beam end is considered on the n_{elem}th element.

2.3 Chatter state

Collision, which induces the chatter state, can occur under three major conditions. The first and second conditions each comprise three distinct states, whereas the third condition consists of two specific states. The first and second conditions relate to the motion of the buoys in opposite directions, whereas the third condition involves the movement of the buoys in the same direction. In the case where the buoys move in the same direction, it is enough for the slope of the displacement-time graph of the first buoy to exceed the corresponding slope of the second buoy's graph. In other words, for a collision to occur, the tooth must move at a high speed and reach the end of the beam during its motion. The conditions of chatter occurring are detailed as follows:

Condition 1 The simultaneous occurrence of the following three conditions, as expressed by the following equations, is necessary for possible collision between the buoys moving in different directions:

• The velocity of the second buoy must be positive, whereas that of the first buoy should be negative.

$$Z_{1f2}(k)>0>Z_{1f1}(k) \quad (7)$$

• The velocity of the free end of the beam should be less than that of the tooth.

$$W_{\mathrm{relvel}}\left(n_{\mathrm{elem}},k\right)-Z_{1f1}(k)<0 \quad (8)$$

• The absolute deflection of the free end of the beam relative to the reference coordinate system (free surface of the water) should be less than the absolute displacement of the tooth relative to the reference coordinate system.

$$\mathrm{abs}\left(W_{\mathrm{relvel}}\left(n_{\mathrm{elem}},k\right)\right)<\mathrm{abs}\left(Z_{1f2}(k)\right) \quad (9)$$

Condition 2 This condition is analogous to the initial one, with the only difference being that the directions of the buoys are switched. Therefore, the equations for this condition are as follows:

$$Z_{1f1}(k)>0>Z_{1f2}(k) \quad (10)$$

$$W_{\mathrm{relvel}}\left(n_{\mathrm{elem}},k\right)-Z_{1f1}(k)>0 \quad (11)$$

$$\mathrm{abs}\left(W_{\mathrm{relvel}}\left(n_{\mathrm{elem}},k\right)\right)>\mathrm{abs}\left(Z_{1f2}(k)\right) \quad (12)$$

Condition 3 In instances where the buoys move in the same direction, a collision can occur only if the speed of one buoy surpasses that of the other. The specific nature of this collision, which causes the chatter state, is considered in this section. When the velocities of the buoys align, chatter-type collision is possible only when the speed of

the second buoy exceeds that of the first, signifying that the second buoy lags behind the first in terms of spatial positioning. This condition is formulated as follows:

$$\begin{cases} Z_{1f2}(k) - Z_{1f1}(k) > 0 \\ W_{\text{relvel}}(n_{\text{elem}}, k) - Z_{2f2}(k) < 0 \end{cases} \tag{13}$$

2.4 Sticking state

In this scenario, upon contact between the beam and tooth, the tooth adheres to the beam instead of causing vibration. To elaborate, the sticking state is inevitable if neither the free nor the chatter state occurs. In this case, vibration in the beam is impossible, resulting in the piezoelectric not producing any power. Following the entire movement period until the release of the cantilever beams, the sole variable parameter is the height difference between the two buoys, culminating in the transition to the free phase after release.

Having explained the characteristics of the buoys and system, the following section delves into a detailed discussion of their performance. The system under consideration in this study comprises two buoys, as illustrated in Figure (1b). Each buoy possesses a single degree of freedom, exclusively moving along the vertical (Z) axis. Their vertical movement is facilitated by guide rods fixed to a plate. Notably, the first buoy is equipped with a rigid tooth, whereas the second buoy contains a cantilever beam.

3 Results and discussion

This section focuses on the investigation of the effects of key parameters on the proposed system's behavior. These parameters include the fundamental components of the system, namely, the wave, buoys, and cantilever beam connected to the second buoy. Each factor plays a crucial role in shaping the vibrational characteristics of the beam, the dynamic of the buoys, and overall power production by the system.

For comparative analysis, a default mode is established as a baseline to evaluate all subsequent outputs resulting from alterations. The key outputs under examination in this section include output power, buoy oscillation amplitude, and system period. In this context, "period" refers to the harmonic and recurrent motion of buoys repeating at equal time intervals once the system reaches stabilization. Additionally, in accordance with the reference (Lin and Zhang, 2016), the optimal sea wave period is chosen as 1.1 s.

3.1 Default mode

The physical properties of the buoys for the default mode analysis are detailed in Table 1. In this mode, the same dimensions and specifications are assigned to both buoys. Simulations, comprising power output, system period, buoy motion range, and overall system behavior, are conducted to analyze the system's performance in the default mode. The results of the simulations are illustrated in Figure 3, providing a comprehensive depiction of all the observable behavioral states of the system, including free vibration, chatter, and sticking. The simulation duration is 120 s, which is sufficient for simulating these states.

Figure 3(a) presents a detailed depiction of the system's period. This period must be differentiated from the wave period, as illustrated in Figure 3(b). Notably, in Figure 3(b), the beam undergoes charging events 10 times within a complete system period, encompassing instances of the tooth adhering to the beam, its subsequent release, and the free vibrations of the beam. Out of these 10 occurrences, two involve chatter and its consequent vibration, whereas the remaining eight entail the complete adhesion of the tooth to the beam, persisting until the beam reaches its maximum elevation, followed by free vibrations. In Figures 3(c) and 3(d), two distinct types of charging events are depicted: chatter and full sticking (magnified). During the chatter state, the beam experiences heightened vibration, supplementing the free vibrations resulting from its release (Figure 3(c)). The chatter and recharging persist as long as the tooth remains within the range of the beam's maximum deflection. Additionally, as shown in Figure 3(d), the beam undergoes charging in three separate full sticking states.

Table 1 Physical properties of the system in default mode

Buoy diameter		Buoy height		Buoy wetting height	
First D_{f1} (m)	Second D_{f2} (m)	First H_{f1} (m)	Second H_{f2} (m)	First H_{wf1} (m)	Second H_{wf2} (m)
0.3	0.3	0.3	0.2	0.1	0.1
Buoy density		Beam length L (m)	Beam width W (m)	Beam thickness T (m)	Beam Young modulus E (GPa)
First ρ_{f1} (g/cm^3)	Second ρ_{f2} (g/cm^3)				
0.5	0.5	0.136	0.0196	0.00067	190
Beam density ρ_B (g/cm^3)	Beam–tooth overlap L_{ovlp} (m)	Wave period WP (s)			
7900	0.0029	1.1			

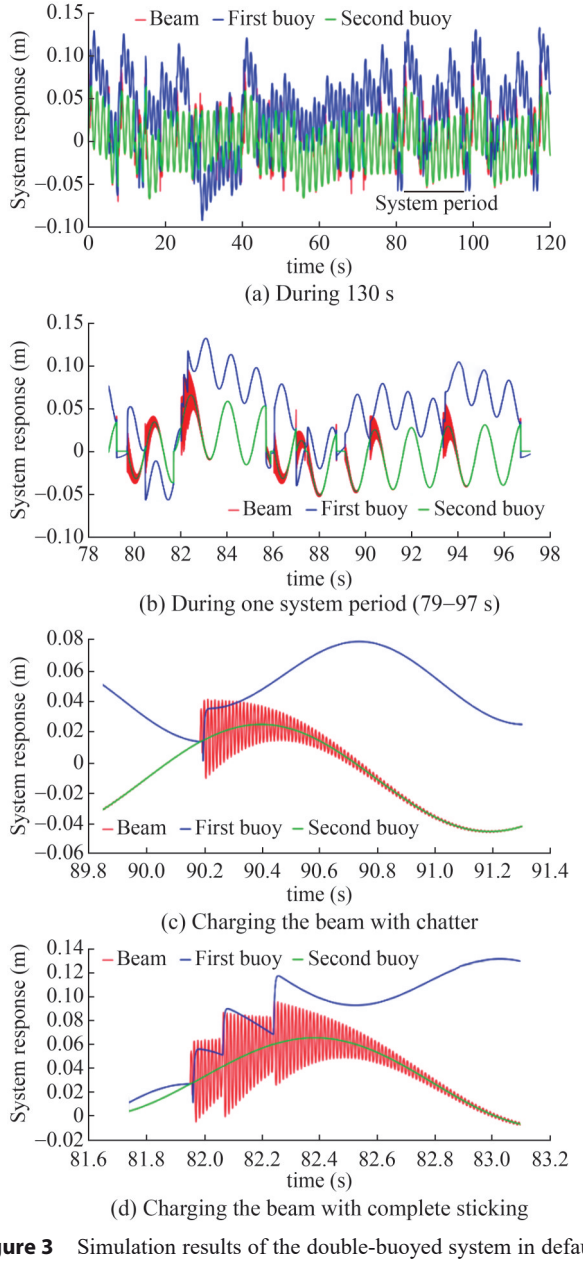

Figure 3 Simulation results of the double-buoyed system in default mode

ing and chatter conditions and utilizing the simulation algorithm developed in this study.

In the diagram in Figure 4(a), which depicts the single-buoyed mode, the maximum deflection of the beam is recorded at 10 mm, with the buoy exhibiting a range of motion spanning 25 mm, as also illustrated in Figure 4(b). Notably, the consequential chatter of the collision reaction between the beam and tooth on the buoy's range of motion is not noticeable in Figure 4(a). Such actions and reactions are inherent in reality but are absent from this representation. However, in Figure 4(b) (derived from the proposed algorithm), the effect of the beam reaction on the buoy becomes evident after each impact. Figure 4(b) shows the slight deviation of the buoy from its trajectory at the moment of impact, an occurrence anticipated in accordance with Newton's third law. This deviation serves as an important validation of the simulation's high accuracy, as presented in this article.

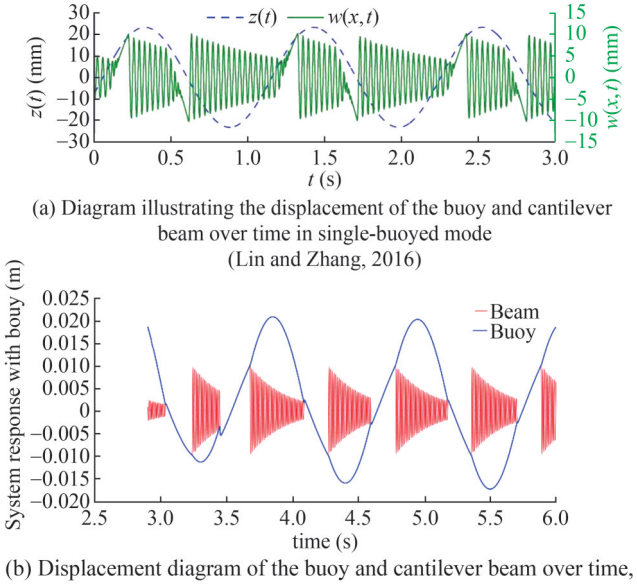

Figure 4 Comparison of the behaviors of the single-buoyed system

Further examining Figure 3 reveals that each impact on the buoy induces a small movement that is typically on the order of a few centimeters. This response underscores the notably high accuracy of the simulation results in predicting the real behavior of the system, particularly when compared with the simulations reported in Lin and Zhang (2016). A comparison is carried out on the basis of Figure 4(a), a diagram extracted from Lin and Zhang (2016), to validate these results. This comparison is accompanied with Figure 4(b), which presents the simulation results of the single-buoyed mode obtained through the simulation algorithm developed in this research. The results are acquired by stabilizing the buoy carrying the tooth while introducing new stick-

Furthermore, the potential variation in the period of the buoys across different states must be considered in evaluating the system's power production. An average power per second is introduced to enable standardized comparison. For the default mode, the cumulative power over the simulation period is 0.577 2 W. This total is then divided by the system period to obtain the average power, which is 0.004 3 W/s during the simulation duration. The energy production in the single-buoyed mode reported in (Lin and Zhang, 2016) is approximately 0.002 1 W. This direct comparison underscores that the double-buoyed system shows an increase in power production, confirming its enhanced efficiency.

3.2 Parametric study on the effect of varying the density of the first buoy on system performance

Changes in buoy density are explored to understand their effect on system behavior. In this study, the density of one buoy (the tooth carrier) is varied, whereas other physical properties are kept constant. Buoy density is varied from 0.5 g/cm³ to different values. The results are illustrated in Figure 5.

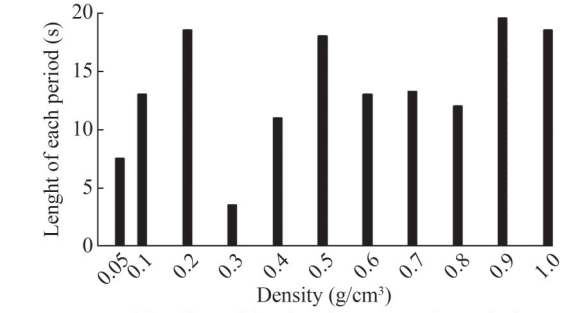

(a) Effect of density changes on the period

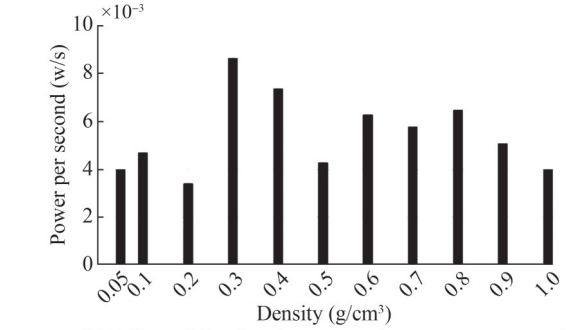

(b) Effect of density changes on the power per second

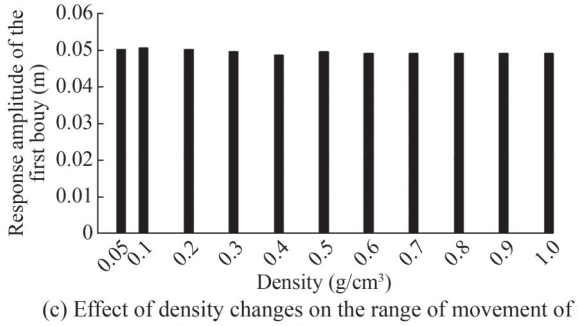

(c) Effect of density changes on the range of movement of the first buoy of the proposed system

Figure 5 Effect of density changes on the period, power per second, and range of movement of the first buoy of the proposed system

Figure 5(a) shows that the overall system period at other buoy densities increases compared with that at the default density of 0.5 g/cm³. This nonlinear increase is attributed to changes in mass, affecting the natural frequency of the buoy carrying the tooth. Figure 5(b) reveals that, in general, high density results in increased average power extraction due to changes in the buoy's momentum upon collision with the beam. Figure 5(c) demonstrates that the buoy maintains movement on sea waves without altering its range. The phenomenon observed in Figure 5(c) is explained by the effect of density on buoyant and hydrostatic forces. It should be noted that mentioned forces themselves are influenced solely by changes in volume. Notably, increased density optimizes system behavior, particularly in enhancing power generation. Given that the density of free ocean water at 20 ℃ is 1.029 g/cm³ on average, buoy density should not surpass this value.

3.3 Parametric study on the effect of changing the diameter of the first buoy on system performance

Similar to the previous analysis, modifications are applied solely to the buoy carrying the tooth. These modifications involve adjusting the diameter of the buoy, deviating from the default diameter of 30 cm. By contrast, all other properties are held constant. The variation in buoy diameter not only affects the mass of the first buoy but also influences the forces exerted on the buoy by sea waves, including buoyant and hydrostatic forces. The outcomes of these changes are illustrated in Figure 6.

Figure 6(a) shows that the overall movement period has significantly reduced. However, the abrupt change observed when the buoy diameters are 30 and 35 cm is attributed to the system's nonlinear nature. Figure 6(b) illustrates the effect of diameter changes on the produced average power. As shown in this figure, when the buoy diameter exceeds 30 cm, the average power also increases. This change is attributed to the direct relationship of buoyancy and hydrostatic forces with the surface area of the buoy. Nevertheless, Figure 6(c) depicts the existence of amplitude changes, indicating that the model's behavior does not follow a consistent trend.

3.4 Parametric study on the effect of sea wave period variations on system performance

As discussed in this section, the default dimensions of the two buoys are maintained, whereas the sea wave period is varied, assuming a deviation from the default period of 1.1 s. This variation represents scenarios of heightened turbulence or increased calmness in the sea. Figure 7 illustrates the analysis results concerning the wave period and its consequential effects on the system.

An evident correlation is observed in Figure 7(a). Specifically, an increase in the wave period corresponds to a prolongation of the system period. This correlation signifies a temporal adjustment in the interaction between the action and reaction of the buoy. Consequently, as illustrated in Figure 7(b), the overall system performance is enhanced in terms of power production. This enhancement is particularly notable from the 3 s period onward, presenting an approximately 40% increase. It can be attributed to the shortening of the wave period by intensified sea turbulence, thereby augmenting the frequency of buoy move-

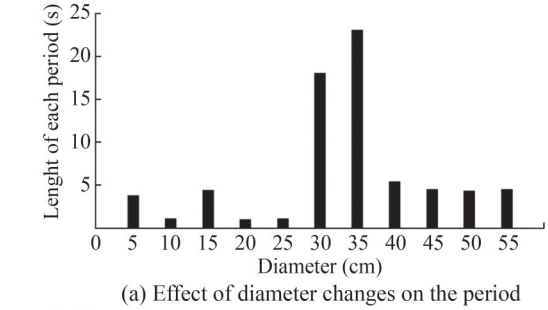

(a) Effect of diameter changes on the period

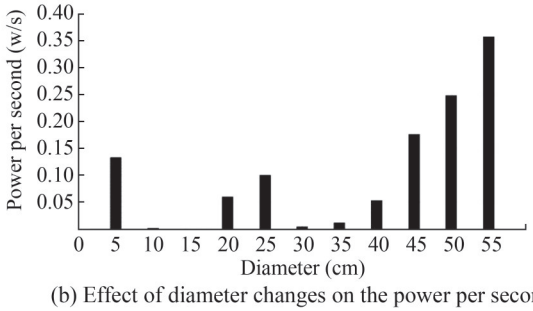

(b) Effect of diameter changes on the power per second

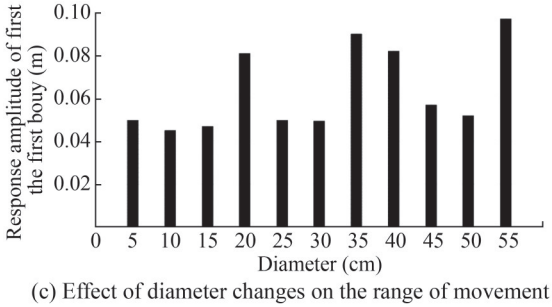

(c) Effect of diameter changes on the range of movement of the first buoy of the proposed system

Figure 6 Effect of diameter changes on the period, power per second, and range of movement of the first buoy of the proposed system

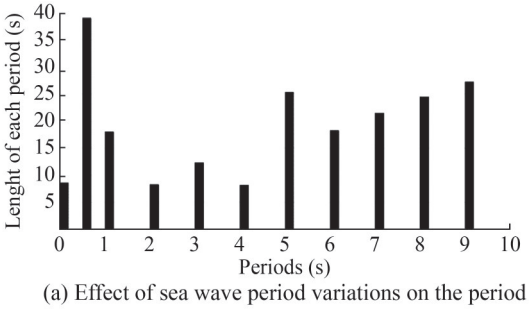

(a) Effect of sea wave period variations on the period

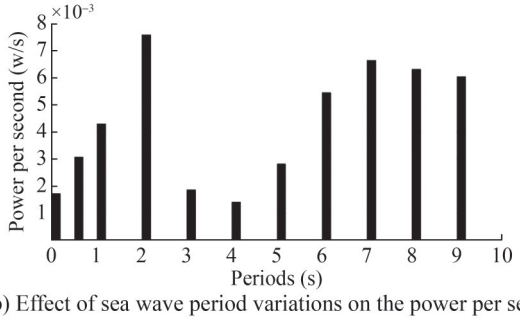

(b) Effect of sea wave period variations on the power per second

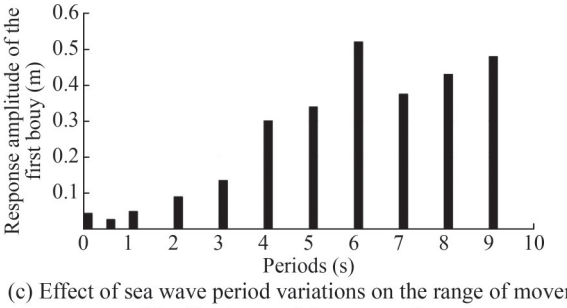

(c) Effect of sea wave period variations on the range of movement of the first buoy of the proposed system

Figure 7 Effect of sea wave period variations on the period, power per second, and range of movement of the first buoy of the proposed system

ments and collisions. This effect, in turn, reduces the free vibration period of the beam, resulting in increased power generation. Figure 7(c) illustrates an expansion in the range of buoy movement, which increases by five times relative to that in the default mode. Frames at two distinct periods, i.e., 0.6 and 1.9 s, are presented in Figure 8 to illustrate the system's behavior.

Although Figure 8(b) does not indicate high frequency, unlike Figure 8(a), it shows that power production by the system has increased, indicating that system performance has improved in terms of power.

3.5 Parametric study on the effect of changing the height of the first float on system performance

Modifying the height of the first buoy (relative to the default height of 20 cm) while keeping the density constant does not affect the center of mass of the buoy. The constant density ensures that the center of mass remains fixed on the water's surface. The outcomes of this modification are illustrated in Figure 9.

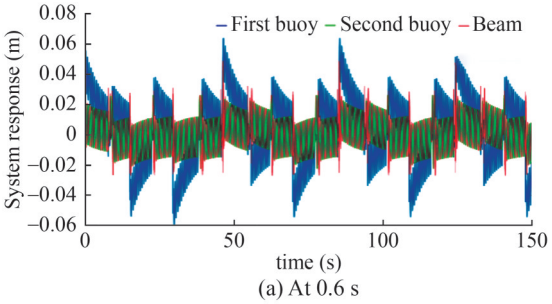

(a) At 0.6 s

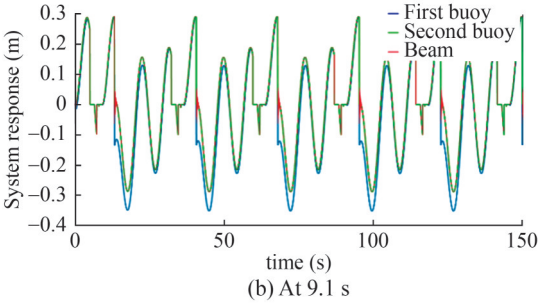

(b) At 9.1 s

Figure 8 Simulation results of the behavior of the proposed double-buoyed system at different periods

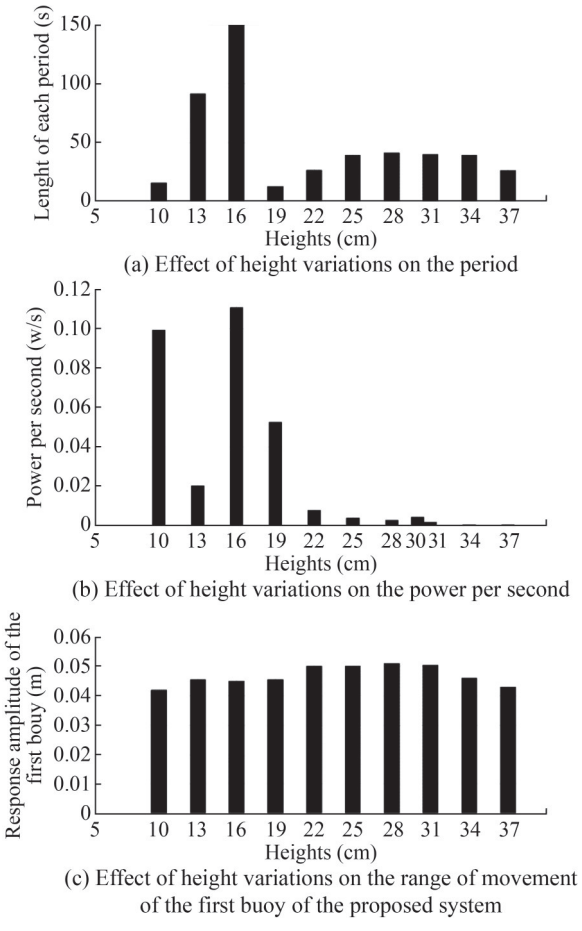

Figure 9 Effect of height variations on the period, power per second, and range of movement of the first buoy of the proposed system

According to Figure 9(a), the system period suddenly increases at 16 cm but uniformly increases starting at 19 cm (with the default height being 20 cm and the system period being 17.5 s). Additionally, Figure 9(b) reveals that power increases at 10 and 16 cm but noticeably decreases at a height of 19 cm. This behavior is attributed to the effect of the first buoy's height on kinetic momentum and system damping, given that an increased wetting surface enhances hydrostatic and buoyancy forces, resulting in a reduction in the first buoy's speed and period duration. Therefore, an increase in height appears to lead to a decline in system power. Figure 9(c) illustrates that the change in the range of motion remains relatively consistent.

3.6 Maximum power mode

As described in this section, the optimal values of the system parameters, derived from the steps of the parametric analysis (Sections 3.2–3.5) reported in each subsection, are selected to maximize power output. The results are depicted in Figure 10. All dimensions in the maximum power mode are held equal to those in the default state, whereas density, height, and diameter are adjusted to 0.3 g/cm³, 16 cm, and 55 cm, respectively.

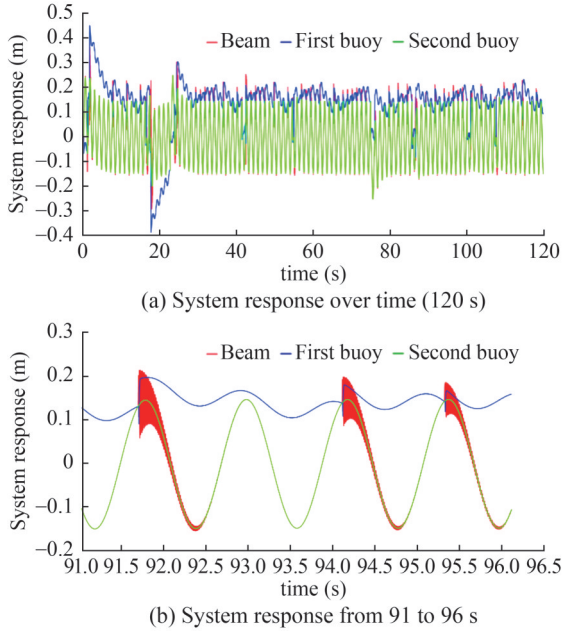

Figure 10 Simulation results for the maximum power mode

According to Figure 10(a), the average power output of the system in the maximum power mode is 0.056 W/s. The power production rates of the single-buoyed and proposed systems are 0.002 1 and 0.004 3 W/s, respectively.

4 Conclusions

This work proposes a novel double-buoyed model for energy harvesting from sea waves through impact. This system overcomes the limitations of previous models while considerably increasing energy output. First, the mathematical model of the new system is constructed. The governing equations of the system are then extracted. Furthermore, a newly developed computer algorithm is employed to solve equations and acquire the dynamic responses of the proposed system. The main results of this study are as follows:

1) System dynamics involve interaction between the beam and tooth, leading to beam vibration and generating power. Impact increases beam frequency, particularly piezoelectric frequency, converting very low sea wave frequencies into high frequencies (hundreds of Hz). The substantial increase in electricity generation is achieved through the embedded piezoelectric elements on the beam.

2) Compared with that of a previous single-buoyed system, power production by the newly developed system has enhanced to 0.004 3 from 0.002 1 W/s.

3) The main vibrating frequency of beams is up-con-

verted into high frequency from slow buoy motion through transformation, and frequency mainly depends on system physical parameters and wave parameters. Therefore, the effect of key parameters of the proposed system, such as density, the diameter and height of the first buoy, and the wave period, are investigated on the basis of the average produced power per second and buoy movement range. Parametric analysis identifies optimal values for the parameters that substantially increase power output. Finally, the selected parameters are found to result in a noticeable increase in the power output of the double-buoyed system from 0.004 3 to 0.055 6 W/s, representing a nearly 13-fold improvement.

Moreover, this study uses the regular airy wave model. In future works, the dynamic behavior of the proposed system should be investigated in consideration of random JONSWAP wave theory.

Competing interest The authors have no competing interests to declare that are relevant to the content of this article.

References

Bao B, Tao J, Liu J, Chen J, Wu Y, Wang Q (2022) Energy harvester using two-phase flow conditions. Energy Conversion and Management 273: 116405. https://doi.org/10.1016/j.enconman.2022.116405

Chen J, Bao B, Liu J, Wu Y, Wang Q (2022) Piezoelectric energy harvester featuring a magnetic chaotic pendulum. Energy Conversion and Management 269: 116155. https://doi.org/10.1016/j.enconman.2022.116155

Chen SE, Yang RY, Wu GK, Wu CC (2021) A piezoelectric wave-energy converter equipped with a geared-linkage-based frequency up-conversion mechanism. Sensors 21(1): 204. https://doi.org/10.3390/s21010204

Cummins W (1962) The impulse response function and ship motion. David W. Taylor Model Basin, Hydromechanics Laboratory Research and Development Report

Du X, Chen H, Li C, Li Z, Wang W, Guo D, Yu H, Wang J, Tang L (2024a) Wake galloping piezoelectric-electromagnetic hybrid ocean wave energy harvesting with oscillating water column. Applied Energy 353(Part A): 122081. https://doi.org/10.1016/j.apenergy.2023.122081

Du X, Li P, Li Z, Liu X, Wang W, Feng Q, Du L, Yu H, Wang J, Xie X (2024b) Multi-pillar piezoelectric stack harvests ocean wave energy with oscillating float buoy. Energy 298: 131347. https://doi.org/10.1016/j.energy.2024.131347

Falnes J, Kurniawan A (2020) Ocean waves and oscillating systems: linear interactions including wave-energy extraction, Cambridge: Cambridge University Press

Jahangiri V, Mirab H, Fathi R, Ettefagh M (2016) TLP structural health monitoring based on vibration signal of energy harvesting system. Latin American Journal of Solids and Structures 13(5): 897-915. DOI: 10.1590/1679-78252282

Hoffmann D, Willmann A, Hehn T, Folkmer B, Manoli Y (2016) A self-adaptive energy harvesting system. Smart Materials and Structures 25(3): 035013. https://doi.org/10.1088/0964-1726/25/3/035013

Lin Z, Zhang Y (2016) Dynamics of a mechanical frequency up-converted device for wave energy harvesting. Journal of Sound and Vibration 367: 170-184. https://doi.org/10.1016/j.jsv.2015.12.048

Mirab H, Fathi R, Jahangiri V, Ettefagh MM, Hassannejad R (2015) Energy harvesting from sea waves with consideration of airy and JONSWAP theory and optimization of energy harvester parameters. Journal of Marine Science and Application 14: 440-449. https://doi.org/10.1007/s11804-015-1327-5

Mohapatra SC, Guedes Soares C (2024) Oblique wave interaction with an integrated wave energy extraction system. Innovations in Renewable Energies Offshore. Boca Raton: CRC Press 835-843

Nan W, He Y, Fu J (2021) Bistable energy harvester using easy snap-through performance to increase output power. Energy 226: 120414. https://doi.org/10.1016/j.energy.2021.120414

Ramezanpour R, Nahvi H, Ziaei-Rad S (2016) Electromechanical behavior of a pendulum-based piezoelectric frequency up-converting energy harvester. Journal of Sound and Vibration 370: 280-305. https://doi.org/10.1016/j.jsv.2016.01.052

Wang S, He L, Wang H, Li X, Sun B, Lin J (2024) Energy harvesting from water impact using piezoelectric energy harvester. Review of Scientific Instruments 95: 021501. https://doi.org/10.1063/5.0155633

Wu N, Wang Q, Xie XD (2015) Ocean wave energy harvesting with a piezoelectric coupled buoy structure. Applied Ocean Research 50: 110-118. https://doi.org/10.1016/j.apor.2015.01.004

Xie XD, Wang Q (2017a) A study on an ocean wave energy harvester made of a composite piezoelectric buoy structure. Composite Structures 178: 447-454. https://doi.org/10.1016/j.compstruct.2017.06.066

Xie XD, Wang Q (2017b) A study on a high efficient cylinder composite piezoelectric energy harvester. Composite Structures 161: 237-245. https://doi.org/10.1016/j.compstruct.2016.11.032

Xie XD, Wang Q, Wu N (2014) Energy harvesting from transverse ocean waves by a piezoelectric plate. International Journal of Engineering Science 81: 41-48. https://doi.org/10.1016/j.ijengsci.2014.04.003

Xu G, Shen W, Wang X (2014) Applications of wireless sensor networks in marine environment monitoring: a survey. Sensors 14(9): 16932-16954. https://doi.org/10.3390/s140916932